The Role of Alkali Metal Cations on Electronic Structure and Halide Segregation of Hybrid Perovskites

Siyuan Zhang,[†^*] *Ming-Chun Tang,*[†‖§] *Yuanyuan Fan,*[‡] *Ruipeng Li,*[¶] *Nhan V. Nguyen,*[†] *Kui Zhao,*[‡] *Thomas D. Anthopoulos,*[‖*] *Christina A. Hacker*[†*]

[†]Physical Measurement Laboratory, National Institute of Standards and Technology (NIST) Gaithersburg, MD 20899, USA

[‖]King Abdullah University of Science and Technology (KAUST), KAUST Solar Center (KSC), and Physical Science and Engineering Division (PSE), Thuwal, 23955-6900, Saudi Arabia.

[‡]Key Laboratory of Applied Surface and Colloid Chemistry, National Ministry of Education, Shaanxi Key Laboratory for Advanced Energy Devices, and Shaanxi Engineering Lab for Advanced Energy Technology, School of Materials Science and Engineering, Shaanxi Normal University, Xi'an 710119, China.

[¶]Brookhaven National Laboratory (BNL), Upton, NY 11973, USA.

[§]Institute for Research in Electronics and Applied Physics & Maryland NanoCenter, University of Maryland, College Park, MD 20742, USA

[^] Theiss Research, La Jolla, CA 92037, USA

S. Z. and M-C. T. contributed equally to this work.

KEYWORDS: mixed-cation and mixed-halide perovskites, band structure, depth profile, microstructure, phase segregation

ABSTRACT

The ability to control or prevent phase segregation in perovskites is crucial to realizing stable and tunable mixed-halide optoelectronic devices. In this work, we systematically examine the impact of alkali metal cation (Cs^+ and K^+) concentration on band structure, chemical composition, phase segregation, and polycrystalline microstructure on formamidinium-dominated mixed-halide mixed-cation perovskite films. It was found that the incorporation of Cs^+ and K^+ cations decreases the work function and the core levels of all components shift toward higher binding energy consistent with n-doping the perovskite film, which facilitates electron transfer to the electron transport layer TiO_2. A concentration-dependent film structure was observed by X-ray photoemission spectra and grazing incidence wide-angle X-ray scattering where the halides and cations are distributed evenly across perovskite films at low metallic cation concentration (5 %). A high metal cation ratio (20 %) leads to halide segregation within the perovskite film and the surface becomes bromide-poor while the bromide and metal cations diffuse to deeper within the film. These differences in electronic properties, element distribution, and film morphology were reflected in the device performance where the power conversion efficiency of low metallic cation concentration (5 % of Cs^+ and K^+) perovskite solar cells is ≈5 % higher than the high concentration ones (20 %). This study provides valuable chemical and physical insight into the underlying trade-offs in the careful tuning of electrical properties and film structure to optimize multi-cation and mixed-halide hybrid perovskites.

INTRODUCTION

The hybrid mixed-cation lead mixed-halide perovskite materials have attracted much attention in the solar cell community due to remarkable characteristics, including high absorption coefficient, low exciton binding energy, high carrier transport, high power conversion efficiency (PCE), and low-cost solution-processable fabrication.[1-6] Organic-inorganic trihalide perovskites feature the characteristic AMX_3 structure. Suitable A cations to form perovskites are organic or inorganic monovalent cation, most often methylammonium (MA^+), formamidinium (FA^+), cesium (Cs^+), potassium (K^+), rubidium, or a mixture. M is a metal cation such as lead (Pb^{2+}) or tin (Sn^{2+}), and X is a monovalent anion such as chloride (Cl^-), bromide (Br^-), iodide (I^-), or a mixture.[7-9] To date, solution-processed small-scale planar heterojunction perovskite solar cells with a certified PCE surpassing 25 %, have been reported.[10] Despite the current success of single-cation mixed-halide MA^+-based perovskites for photovoltaic applications, these perovskites are thermally unstable and tend to form halide segregation.[3] FA^+-based perovskites have better thermal stability but suffer from the phase instability where a cubic structure is formed from a trigonal structure.[11] Compositional engineering of perovskite semiconductors by introducing mixed halides and cations has been widely used to tune the bandgap, balance the electron and hole transport in photovoltaics, improve uniformity and stability, and achieve highly efficient perovskite solar cells.[12, 13] The use of FA^+ and MA^+ mixed cations perovskite with the structure of $(FAPbI_3)_{1-x}(MAPbBr_3)_x$ have resulted in solar cells with efficiency over 20 %.[14] It has been reported that the incorporation of alkali metal cations into the A^+ site promotes the stability and reproducibility of the efficiency of perovskite solar cells by inhibiting the creation of the δ phase. For instance, the incorporation of a small number of metal cations, such as K^+ and Cs^+, results in a slightly wider bandgap and can further improve crystal growth and morphology of the films, and improve thermal and moisture

stability.[15-20] The triple cation-based (Cs^+/ FA^+/ MA^+) perovskite films achieve over 21 % PCE with stable performance after long time exposure to the ambient atmosphere.[15] Previous studies have reported that passivated triple-cation (Cs, FA, MA)$Pb(I_{0.85}Br_{0.15})_3$ perovskite thin films with additional potassium cation incorporation could substantially mitigate both non-radiative losses and photoinduced ion migration in perovskite films, resulting in enhanced performance of solar cells and light-emitting diodes.[19] The ability to control or prevent photoinduced phase segregation in perovskites is crucial to realizing stable and tunable mixed-halide optoelectronic devices. Despite the achievement of high-performance solar cells consisting of mixed cations and halides perovskites, the in-depth roles of alkali metal cations on electronic structure, chemical composition, microstructure, and the mechanisms that form the basis for improved performance and stability through precursor stoichiometry engineering are still poorly understood.

Herein, we focus on interface and phase segregation problems in triple-cation perovskite thin films and systematically characterize the electronic structure and chemical compositions of alkali metal ions (Cs^+ and K^+) incorporated into mixed-cation perovskites and determine the distributions of metal cations and halides in perovskite layers. Perovskite phase segregation is typically observed using techniques such as absorption and photoluminescence spectroscopy, external quantum efficiency, transient difference absorption spectroscopy, and photovoltaic performance.[21-24] However, these techniques are indirect and probe the optical and electrical properties rather than information regarding the spatial distribution. Here, the depth-profile X-ray photoemission spectra (XPS) data directly prove the existence of the bromide-poor phase located close to the film surface and bromide-rich phase presented close to the substrate. This is the first report of direct observation of phase segregation in the triple-cation hybrid perovskite system using XPS. Perovskite films with formulation $FA_{0.85-x}MA_{0.15}M_xPbI_{2.55}Br_{0.45}$, where M = Cs^+ or K^+ and

x varies from 0 (non-metal ion perovskite), 0.05, 0.1, to 0.2. These films abbreviated as M0, Cs5, K5, Cs10, K10, Cs20, and K20, respectively. The optical absorbance and ultraviolet photoelectron spectra (UPS) of mixed-cation films show that the band structure shifts are strongly correlated to alkali metal ion concentration and the position of conduction band minimum (CBM) raises which facilitates electron transfer. In-depth analysis of film composition and microstructure indicate the presence of perovskite halide segregation occurred at high alkali metal cation concentration, while low-concentration alkali cation perovskite layers exhibited halides, lead, and multiple cations distributed homogeneously across the film. The phase segregation in the triple-cation hybrid perovskites was also confirmed by grazing incidence wide-angle X-ray scattering (GIWAXS). These differences in electronic structure, chemical composition, and polycrystalline microstructure were reflected in device performance: higher average PCEs were demonstrated with low Cs^+ incorporated perovskite solar cells (>19.2 % for Cs5 and Cs10) than high Cs^+ concentration film (≈14.7 % for Cs20). Similar trends were observed in K^+ incorporated perovskite system. This work helps to elucidate the limitations of adding alkali metal halides, and the information and understanding about the electronic structure and composition of triple-cation perovskites with mixed halides can be used to guide the synthesis of new perovskite films with uniform composition to improve performance in optoelectronic applications.

RESULTS AND DISCUSSION

To study the effects of alkali metal ion substitution on the properties of $APbX_3$ ($X = I_{0.85}Br_{0.15}$) perovskite films, the precursor solutions were prepared at the desired reaction ratios and then spin-coated on the substrate using the one-step deposition protocol (see *Experimental Details*). The resulting films of $A_{1-x}Cs_xPbX_3$ and $A_{1-x}K_xPbX_3$ (x = 0, 0.05, 0.1, and 0.2) are abbreviated as M0,

Cs5, K5, Cs10, K10, Cs20, and K20, respectively, and X is a mixture of halides ($X = I_{0.85}Br_{0.15}$) with the same ratio throughout this study.

The optical properties of the mixed-cation perovskite films with mixed halides were characterized using absorption spectroscopy. **Figure 1**a shows the optical absorbance spectra of thin films with the composition varying from 5 % to 20 % of K^+ and Cs^+ cations. The concentration of K^+ has little impact on the absorbance. The bandgaps were calculated to be ≈1.6 eV, while a higher concentration of Cs^+ blue shifts the spectra and increases the bandgap from ≈1.61 eV to ≈1.85 eV. In order to map the band structure as a function of the alkali metal ion content, we investigate the energetics of the occupied states by using UPS. The work function ϕ and the position of valance band maximum (VBM) relative to the Fermi level (E_f) can be determined by UPS. Figure 1b shows the high binding energy cutoff regions (i.e., secondary electron edge, SEE) and the low binding energy part of the UPS spectra close to the Fermi energy (E_f = 0 eV) for representative samples. The work function is given by the difference between the energy of the UV photons (21.21 eV for the He I radiation used here) and the binding energy of the secondary electron edge (SEE) ($E_f = E_{He(I)} - E_{SEE}$). The standard deviation from averaging the results obtained with different samples and spots were summarized in Supporting Information (**Table S1**). The corresponding energy diagram of mixed cations perovskites is summarized in Figure 1c. The work function of Cs5 is about 4.56 eV, similar to previous reports.[25] The Fermi level of Cs5 film is located ≈1.42 eV above the VBM and in the upper half of the bandgap (the bandgap is ≈1.61 eV), representing the n-type nature of perovskite film. With increasing Cs^+ concentration in Cs10 and Cs20, we observe a slight increase of VBM level to the higher binding energy of 1.45 eV. The SEE, however, does not shift with Cs^+ concentration consistent with the pinning of the work function at 4.56 eV, a decrease of 0.17 eV compared with no M^+ cations film (M0). In the case of

K^+-incorporated films, the work function is pinned at ≈4.37 eV, a 0.36 eV decrease, with little variation in the VBM level as a function of the K^+ concentration. Similar to Cs^+ films, the K^+ films are n-type with the Fermi levels shifted ≈1.5 eV from the VBM. In all cases, the Fermi level is close to the conduction band minimum represents the n-type nature of these films. The position of the CBM, E_{CBM}, can be calculated from the equation: $E_{CBM} = E_{VBM} + E_{bandgap}$. Incorporation of Cs^+ into the perovskite films leads to a decrease of CBM compared with M0 (CBM ≈4.4 eV for Cs5 and Cs10, CBM ≈4.2 eV for Cs20). Incorporation of K^+, on the other hand, decreases both the VBM and CBM by ≈0.1 eV (compared with M0) and the E_F shifts to ≈4.4 eV for K5, K10, and K20. As reported in the literature, the CBM of porous TiO_2 is ≈4.1 eV.[26, 27] The electronic structure mapped out using UPS and UV-Vis confirms that the rise of the CBM position caused by the incorporation of metal cations facilitates the electron transfer to the electron transport layer, such as TiO_2. The determination of the energetic levels of these perovskite films can unravel the role of band alignment in charge transport.

To further explore the effects of the alkali metal ion content, XPS was used to examine elemental composition. **Figure 2** shows the evolution of XPS C 1s, Pb 4f, I 3d, Br 3d, K 2p, and Cs 4d as a function of alkali metal cation species and concentration. The spectra are normalized to the same height for clarity. The elements are fitted by Lorentzian-Gaussian peaks. The C 1s core-level spectra of all of the films contain three components which are consistent with the previous report: the ≈284.5 eV component is assigned to surface absorbed amorphous carbon, the 285.9 eV and 287.7 eV components are attributed to the C-N bond in MA^+ and FA^+ cations, respectively.[28, 29] The Pb 4f in M0 film shows a sharp doublet located at 137.9 eV (Pb $4f_{7/2}$) and 142.8 eV (Pb $4f_{5/2}$), respectively, which are assigned to Pb^{2+} metal ion. The peak positions of I $3d_{5/2}$ and Br $3d_{5/2}$ located at 618.8 eV and 68.0 eV are also consistent with the literature reports.[28] Both I $3d_{5/2}$ and

Br $3d_{5/2}$ core level include one single peak indicating the halides are present as only one chemical species in the perovskite films. As shown in Figure 2a and 2d, the increased alkali metal cation concentrations can be observed next to C 1s and Br 3d peaks because of the higher content of K 2p and Cs 4d in the perovskite films. We find that the binding energies (BE) of elemental core levels shift to higher (≈0.24 eV) BE as the alkali metal cation concentration increases, which follows the trend in the UPS data shown in Figure 1. This upshift is also consistent with previous studies of Cs^+- and K^+-contained mixed-cation perovskite films.[27, 30] These upshift of both the core levels from XPS and VBM from UPS indicate slightly n-doping of the films as the Fermi level shifts toward the conduction band edge.

To further analyze the distribution of components throughout the film, both angle resolved-XPS (AR-XPS) and depth-profile XPS were conducted for all seven perovskite films. XPS data are limited by the escape depth of photoelectrons, which is typically 10 nm or less, and as the films are rotated away from the surface normal, the effective sampling becomes thinner (≈2.6 nm), thereby probing more of the surface region. The AR-XPS (**Figure S1**) data show that I 3d and alkali metal component (Cs 3d and K 2p) for both Cs5 and K5 films increases as the take-off angle increase from 0 to 75° indicating that there are more iodide and alkali metal cations at the surface rather than the bulk of the perovskite films. The Br 3d, on the other hand, has a higher concentration in bulk than the surface region. The atomic ratios obtained from the AR-XPS for Cs10, Cs20, K10, and K20 showed a similar trend. To get a better idea of film distribution, XPS data were acquired after sputtering with the sputtering rate controlled to ≈ 0.26 nm s^{-1} (refer to *Experimental Details*) to minimize sputtering-induced physical damage. The interfacial region between the perovskite film and the substrate was determined by the abrupt decrease of Pb 4f signal with the increase of O 1s and Sn 3d signals from the substrate. The film thicknesses were

measured by the profilometer and ellipsometry and are reported in the Supporting Information (**Table S2** and **Figure S2**). **Figure 3** illustrates the perovskite film elemental composition as a function of depth profile collected with XPS by using *in situ* Ar^+ sputtering. The sputtering time was converted to sampling depth with the assumption that the etching rate was constant. The depth profiles of Cs5 (Figure 3a) and K5 (Figure 3d) are shown as an example. Surface absorbed amorphous carbon is evident on the top surface and no other surface contamination is observed. The C 1s fraction is reduced mainly after the first sputter and the Pb 4f and I 3d fractions from the perovskite layer increase. To better present the film composition, the atomic ratio of halides (I 3d and Br 3d) and metal cations (Cs 3d or K 2p) is normalized to lead Pb^{2+} (Pb 4f) for the Cs5, Cs20, K5, and K20 films and summarized in Figure 3b-c and e-f. The profiles for other films are presented in the Supporting Information (**Figure S3**). Both Cs5 and K5 present homogeneously distributed atomic ratios across the film thickness. The I/Pb ratios in Cs20 and K20 films decrease from ≈3.2 at the surface to ≈2.4 within the film accompanied by increasing of the Br/Pb ratios from ≈0.25 at the surface to ≈0.5 as the depth increases, suggesting a bromide-poor phase was formed close to the film surface and bromide-rich phase was presented close to the substrate. The alkali metal cations also aggregate with the bromide and higher Cs^+ and K^+ concentration were observed at the bottom of the film. These data show that a small concentration of alkali metal cations results in a relatively homogeneous distribution of cations and halides, but high metal ion concentrations (20 % in this case) can lead to the formation of halide segregation. This is consistent with recent reports that a high alkali metal cation fraction can lead to halide inhomogeneity and phase segregation observed by X-ray fluorescence and transient absorption spectroscopy mapping.[31, 32] Previous studies propose that phase segregation is rooted in halide migration of mixed-halide perovskites, where the lattice strain drives halide segregation for relatively iodine-

rich domains nucleation, changing perovskite composition and lattice structure and resulting in non-uniform composition distribution.[33, 34] Either light illumination or electrical injection generated excited-state charge carriers can couple with the soft lattice to generate a polaron, which results in lattice strain and lead to phase segregation. [29] In this Cs^+ and K^+ metal cations doped mixed-cation perovskite system, a small number of metal cations was effective in preserving FA^+ in its photoactive black perovskite phase due to the significant size difference between Cs^+ and FA^+ ions. However, as the doping level increases, the metal cations aggregate in the form of clusters, which can introduce more lattice strain and destabilize the perovskite phase.

Figure 4 displays the representative scanning electron microscopy (SEM) images of six films and the photographs of each perovskite thin film are shown as insets in each image. The SEM images show that lower concentration (5 %, Figure 4a and d) of both K- and Cs-incorporation leads to the formation of continuous and uniform films, while the films with highest metal ion concentration (20 %, Figure 4c, and f), especially for K20, leads to the formation of needle shape grains and pinholes. Meanwhile, the SEM image of Cs10 (Figure 4b) shows similar morphology to Cs5, but the case of K10 (Figure 4e) demonstrates pinholes and cracks. To compare the morphology with the sample without alkali metal doping (M0, **Figure S4**), the top-view SEM image was also demonstrated in Supporting Information. The origin of these pinholes and cracks is not entirely understood but is likely due to the nucleation and growth behavior of intermediate phases other than the perovskite phase; intermediate phases exhibiting different unit cell sizes can crack upon transformation into the perovskite phase. The incorporation of Cs^+ and K^+ at low concentration promotes the crystallization and grain growth occurs while high alkali metal cation concentration tends to form pinholes and rougher surface.

Next, we employed GIWAXS to investigate the microstructure of the polycrystalline hybrid perovskite layers.[16, 35-41] To understand the impact of different metal ion concentrations on perovskite microstructure, we performed the GIWAXS measurements on Cs5 and Cs20 perovskite films. The length of the scattering vector q is determined by the following equation: $q = \sqrt{q_z^2 + q_{xy}^2}$, where: $q_z = \frac{4\pi sin\alpha_f}{\lambda}$, $q_{xy} = \frac{4\pi sin\theta_f}{\lambda}$, where λ is the wavelength.[42-44] The emergent waves with the momentum can be described by the in-plane exit angle α_f and the out-of-plane angle θ_f (with respect to the scattering plane).[45] To probe and distinguish the differences of perovskite films, **Figure 5**a and c show representative 2D GIWAXS snapshots with scattering vector q versus intensity distribution of these perovskite films for Cs5 and Cs20 respectively. We adopt the widely used nomenclature for metal oxide perovskites proposed by Gratia *et al.* to specify the crystal structure of phases associated with the formation of perovskite thin films.[46, 47] For example, the cubic 3C perovskite phase (acronym 3C) refers to the well-established Ramsdell notation widely used for describing oxide perovskite polytypes[48], is often referred to as α phase. As shown in Figure 5a and b, Cs5 film forms the desired single perovskite 3C phase showing the scattering of (100) at q = 10.21 nm^{-1} with homogeneously well-mixed halide mixture, where the q value of the (100) peaks locates between α_1 and α_2 phases. This observation suggests that a small amount of Cs^+ is unhindered to nucleate and grow the entropically stabilized well-mixed halides 3C (100) phase and may also prevent the segregation of halides and cations. In the case of Cs20 (Figure 5c and d), however, two diffraction features appear close to the 3C (100) perovskite: a Br-poor 3C perovskite α_1 phase at q = 9.92 nm^{-1} and a Br-rich 3C perovskite α_2 phase (at q = 10.28 nm^{-1}). These results prove that uneven mixed halides distribution occurs in the Cs20 perovskite solid-state film, resulting simultaneously in both Br-poor and Br-rich 3C structures. This leads to perovskite 3C phases exhibiting different energetics and bandgaps, which can act as recombination

sites with a negative impact on the performance of solar cells. Figure 5e illustrates the phase segregation as the alkali metal cation concentration increases. Both GIWAXS and XPS confirm that alkali metals are beneficial at low concentrations, where they homogenize the halide distribution, but at higher concentrations, they induce the phase segregation and form recombination-active clusters.

The differences in electronic properties, combined with the differences in film composition and morphology, are expected to result in differences in device properties. The photovoltaic properties of these triple cation-based perovskite films were investigated and the schematic diagram of the solar cell was demonstrated (**Figure 6**a). As summarized in Figure 6b and **Table 1**, the PCE for M0 without any metal ions is 16.88 ± 0.84 %. Incorporation of Cs^+ leads to an enhancement of device performance: Cs5 exhibits a PCE of 19.24 ± 0.53 %, with open-circuit voltage (V_{OC}) of 1.12 ± 0.01 V, short-circuit current (J_{SC}) of 22.77 ± 0.27 mA cm^{-2}, fill factor (*FF*) of 75.50 ± 1.92 %. As the Cs^+ concentration increases, Cs10 shows similar device performance of 19.45 ± 0.40 % and Cs20 exhibits a decreased PCE of 14.63 ± 1.30 %. Similar results were observed for K^+ incorporated solar cells: the average PCE increases slightly to ≈17.15 % for K5, then decreases to ≈15.04 % and ≈12.04 % for K10 and K20, respectively. This decreased PCEs in high Cs^+ and K^+ concentration films are consistent with previously mentioned XPS, SEM, GIWAXS results, and other reports of the device performance of metal cation incorporated perovskite films, [15,27] where the non-uniform composition distribution and pinholes in high metal cation concentration films may behave as recombination sites. Our studies prove that a small amount of Cs^+ and K^+ (≈5 %) can induce highly uniform perovskite grains and improve the device performance, while high metal ion concentration leads to the heterogeneous distribution of metal ion and halide phase segregation, which may deteriorate the device performance. This study

provides in-depth insights into the underlying factors in tuning the electrical properties and film chemical composition by varying the alkali metal cations concentration, which is essential for future perovskite design to achieve enhanced PCE and large-scale production of hybrid perovskite solar cells.

CONCLUSION

In summary, we systemically investigated the effects of alkali metal cation ratios on electronic structure, composition, and microstructure of FA^+-dominated mixed-cation mixed-halide perovskite films. We unravel the crucial roles of Cs^+ and K^+ (small amount, ≈5 %) in promoting homogeneous composition distribution vertically in perovskite films, thus preventing segregation of halides and cations. It was found that the incorporation of metal cations decreases the work function, shifts the Fermi level away from the VBM, and raises the position of the CBM, which facilitates electron transfer to the electron transport layer TiO_2. XPS depth profiling shows that the low alkali metal cation incorporated layers (Cs5 and K5) have uniform elemental mixtures throughout the perovskite structure. In contrast, high alkali metal cation concentration leads to the formation of a bromide-poor phase close to the film surface and bromide-rich phase close to the substrate, showing the existence of halide segregation. These observations were confirmed by GIWAXS in which both Br-poor and Br-rich 3C perovskite phases were observed in Cs20, while only a single well-mixed lead halide perovskite phase was observed in Cs5. Higher efficiencies were demonstrated with Cs5 (≈ 19.24 %) and K5 (≈ 18.57 %) than Cs20 (≈ 14.63 %) and Cs20 (≈ 12.04 %). These results are notable for two reasons. First, both perovskite films and interfaces are significant for highly efficient optoelectronic devices. Here, we have shown that introducing a low metal cation concentration can alter the band structure and facilitate electron transfer. Second, both

XPS and GIWAXS results directly show the importance of delicate control of the phase segregation and elemental distribution with low metal cation concentration, which are crucial to realizing stable and tunable mixed-halide optoelectronic devices. Low concentration alkali metals are beneficial for phase stability, morphology, and device performance, while high concentration alkali metals induce the phase segregation and form recombination-active clusters. This investigation contributes to the fundamental understanding of the mixed-halide mixed-cation perovskites, points to significant guidelines for structural/compositional designing, and paves the path for future perovskite design with improved reproducibility and performance in low-cost and large-scale industrial applications.

EXPERIMENTAL SECTION

Materials: Lead iodide (PbI_2, 99.99 %) was purchased from Alfa Aesar. Lead (II) bromide ($PbBr_2$, 99.99 %), cesium iodide (CsI, 99.9 %), methylammonium bromide (MABr, 98 %), formamidinium iodide (FAI, 99.5%) were purchased from p-OLED.[49] Dimethyl sulfoxide (DMSO, 99.9 %) and N,N-dimethylformamide (DMF, 99.8 %) were purchased from Sigma-Aldrich.[49]

Perovskite layers preparation: The perovskite precursor solution preparation was conducted under an inert atmosphere inside a nitrogen glove box. The precursor solution (1.2 M) was prepared with FAI, MABr, PbI_2, $PbBr_2$, and CsI dissolved in a DMSO and DMF (volume ratio of 4:1) in a glovebox. For example, the $Cs_{0.05}FA_{0.8}MA_{0.15}PbI_{2.55}Br_{0.45}$ precursor solution (1.2 M) was prepared with FAI (0.96 M), MABr (0.18 M), PbI_2 (1.014 M), $PbBr_2$ (0.186 M), and CsI (0.06 M) dissolved in a mixture of DMSO and DMF (4:1 volume/volume) for spin coating. The concentration of the alkali metal ion was controlled by adjusting the alkali metal iodide to the FAI ratio, while the ratio of other precursors, including MABr, PbI_2, $PbBr_2$, remains the same. The ITO-coated glass (2.8

cm×2.8cm) was cleaned by sequential sonication in acetone, isopropanol, and ethanol for 30 min each and then dried under N_2 flow and treated by O_3 plasma for 17 min. The TiO_2 was prepared by chemical bath deposition with the clean substrate immersed in a $TiCl_4$ (CP, Sinopharm Chemical Reagent Co., Ltd) aqueous solution with the volume ratio of $TiCl_4$:H_2O equal to 9:400 at 70 ℃ for 1 hour, its thickness is around 65 nm.[36] The mixed cations perovskite films are processed through a one-step spin-coating method, whereby antisolvent dripping using chlorobenzene (CB) during the spin coating is applied to achieve high-quality polycrystalline perovskite thin films with pure perovskite crystals. Perovskite solutions were spin-coated on top of the TiO_2 layer at 2000 rpm for 10 s with an acceleration of 200 rpm/s. The second step was 4000 rpm for needed time with a ramp-up of 1000 rpm/s. CB (0.2 ml) was dropped on the spinning substrate during the second spin-coating step at 10s before the end of the procedure. The films were then annealed at 100 °C for 10 min. The resulting film is subsequently annealed to acquire the desirable perovskite phase. The perovskite films were coated on ITO glass substrates for the analytical measurements unless stated otherwise.

Photoemission Spectroscopy Measurements. The seven mixed-cation lead mixed-halide perovskite films were transferred into the characterization chamber for ultraviolet and X-ray photoemission spectroscopies (UPS and XPS) to determine the valence band levels and core levels. Angle-resolved XPS was also performed to study the elemental composition and to access the metal ion distribution within the layer. UPS and XPS Spectra were acquired on Kratos Axis Ultra^{DLD} surface analysis system, using the He-I lamp radiation (21.2 eV) and monochromatic Al Kα line, respectively.[50] The films were characterized under a base pressure < 10^{-6} Pa. All samples were in electronic equilibrium with the spectrometer via a copper tape in contact with the perovskite film surface and characterized at a normal take-off angle unless stated otherwise. The

Fermi level was calibrated using sputter cleaned gold film. Survey XPS scans were run at 160 eV pass energy and high-resolution scans at 20 eV pass energy. The UPS spectra were acquired at 5 eV pass energy and 0.05 eV step size with the aperture and iris set to 55 μm. From the binding energy corresponding to the SEE of the UPS spectra we calculated the work function (φ = 21.22 eV – SEE) for each film, and from the onset of photoemission, we determine the position of the valence band maximum. XPS depth profiling was used to investigate the atomic composition at bulk region using an Ar ion gun with power 1 kV and 600 nA on a raster area of 1 mm^2. The XPS spectra were collected after 150 s sputtering time. The sputtering rate is estimated to be 0.26 nm/s, with the assumption that the film thickness is 400 nm and it took 1500 s to fully etch through the film. The film thickness of the films was measured by the profilometer and ellipsometry and the results were shown in the Supporting Information (Table S2 and Figure S2).

Thickness measurement. The film thickness was confirmed by both the profilometry and spectroscopy ellipsometry (SE). The P-7 stylus profiler from Tencor is a surface measurement system with 150 mm scan length standard. We used P-7 stylus Tencor profiler to measure the thickness of hybrid perovskite thin films.[50] SE measurements were performed in a chamber filled with nitrogen gas at room temperature on a vacuum ultraviolet spectroscopic ellipsometer consisting of Xenon and Deuterium lamps covering the wavelength from 140 nm to 1770 nm. The spectroscopic ellipsometer system used in this paper is J. A. Woollam: VUV-VASE VU-302. Photon energy ranging from 1.2 eV to 4.0 eV with 0.01 eV step was scanned during the measurement. The ellipsometry data, Ψ and Δ, were taken at 75° of incidence.

Grazing Incidence Wide-Angle X-ray Scattering (GIWAXS). The GIWAXS experiments were conducted at CMS beamline (11BM) on NSLS II, Brookhaven National Lab. The wavelength of the X-ray was 1.17 Å with a bandwidth of 0.7 %. The scattering signal was collected by a CCD

detector, which was placed 220mm away from the sample with a tilt angle of 19° respect to the X-ray beam. The exposure time was 10s. The data analysis was performed by SciAnalysis.

Optical metrology and morphology analysis. UV-Visible absorption spectra were acquired on a PerkinElmer UV-Lambda 950 instrument. The surface morphology of the perovskite films was characterized by SEM (A Quanta 200FEG SEM).

Solar cell fabrication and characterization. The inverted configuration was adapted with a structure of glass/ ITO/ c-TiO_2/ perovskite/ 2,2′,7,7′-tetrakis-(*N*,*N*-di-pmethoxyphenylamine) 9,9′-spirobifluorene (Sprio-OMeTAD)/ gold (Au). Perovskite solutions were spin-coated on top of the TiO_2 layer at 2000 rpm for 10 s with an acceleration of 200 rpm/s. The second step was 4000 rpm for needed time with a ramp-up of 1000 rpm/s. Chlorobenzene (0.2 ml) was dropped on the spinning substrate during the second spin-coating step at 10s before the end of the procedure. The films were then annealed at 100 °C for 10 min. After cooling down to room temperature, the hole-transporting layer was then deposited on top of the perovskite film via spin-coating at 2000 rpm for 30 s using a the Spiro-OMeTAD solution was prepared by dissolving 90 mg spiro-OMeTAD, 18 µL lithium bis(trifluoromethanesulfonyl) imide (99 %, Acros Organics, 520 mg mL-1) in acetonitrile (99.7 %, Alfa Aesar), 30 µl cobalt dopant (Co TFSI salt, FK209, Anhydrous ACN Sigma Aldrich, the dopant solution should be 300 mg cobalt 3 in 1 ml ACN), and 30 µL 4-tert-butylpyridine (96 %, Aldrich) in 1 mL CB (99.8 %, Aldrich). Finally, 100 nm of gold electrodes were deposited by thermal evaporation using an Angstrom evaporator. The *J-V* performance of perovskite solar cells was analyzed using a Keithley 2400 SourceMeter under ambient conditions at room temperature, and the illumination intensity was 100 mW cm^{-2} (AM 1.5G Oriel solar simulator). The scan range was 2 V – -0.1 V. The scan rate was 0.3 V s^{-1}. The delay time was 50 ms, and the bias step was 0.02 V. Power output of lamp was calibrated using an NREL-traceable

KG5-filtered silicon reference cell. The device area of 0.1 cm^2 was defined by a metal aperture to avoid light scattering from the metal electrode into a device during measurement.

FIGURES

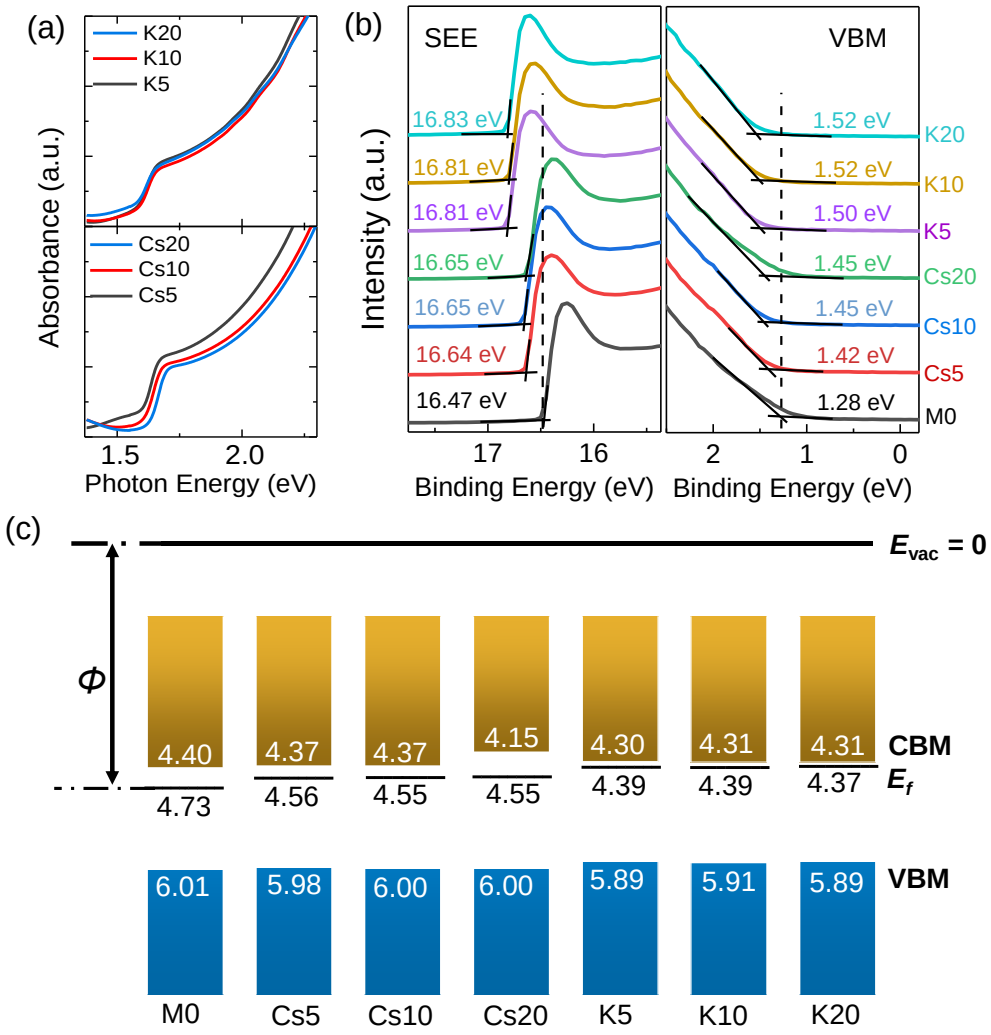

Figure 1. (a) Optical absorbance spectra of K^+- and Cs^+-incorporated mixed cations $A_{1-x}K_xPbX_3$ and $A_{1-x}Cs_xPbX_3$ (x = 0.05, 0.1, and 0.2) perovskite films. (b) UPS SEE and the low binding energy region (near the Fermi energy E_F = 0 eV) of perovskite films with various K^+ or Cs^+ ratio. The onset of ionization of filled states relative to zero binding energy is used to track the shifts of E_F relative to VBM. (c) Schematics of the electronic structure of the mixed-cation and mixed-halide perovskite films near the bandgap region. The average value of the work function (Φ), VBM, and CBM relative to the vacuum level are annotated on the figure. Calculated band energy level according to the UPS and UV−Vis spectra results. The standard deviation from averaging the

results obtained with different samples and spot were summarized in Supporting Information (**Table S1**).

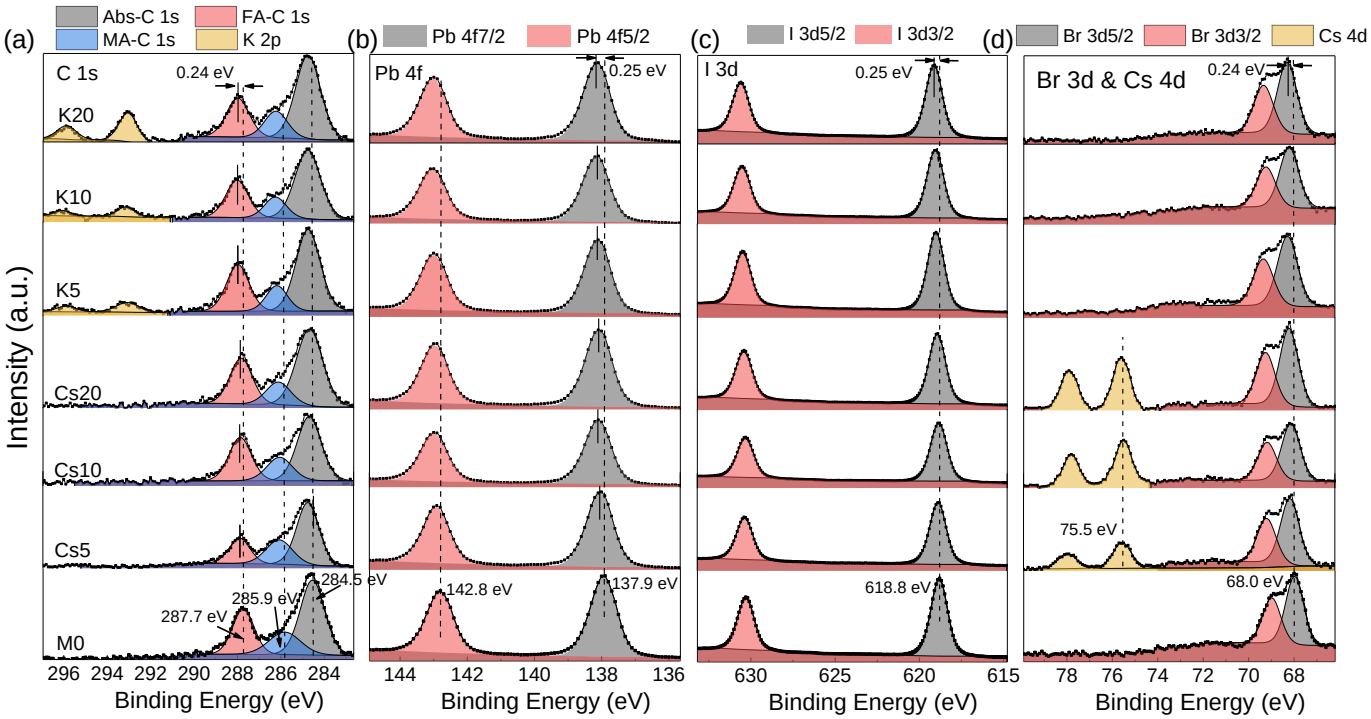

Figure 2. Representative XPS core-level spectra of (a) C 1s and K 2p, (b) Pb 4f, (c) I 3d, (d) Br 3d and Cs 4d for Cs^+- and K^+-incorporated mixed cations $A_{1-x}Cs_xPbX_3$ and $A_{1-x}K_xPbX_3$ (x = 0.05, 0.1, and 0.2) films. The dash lines show the relative shifts of the peak positions.

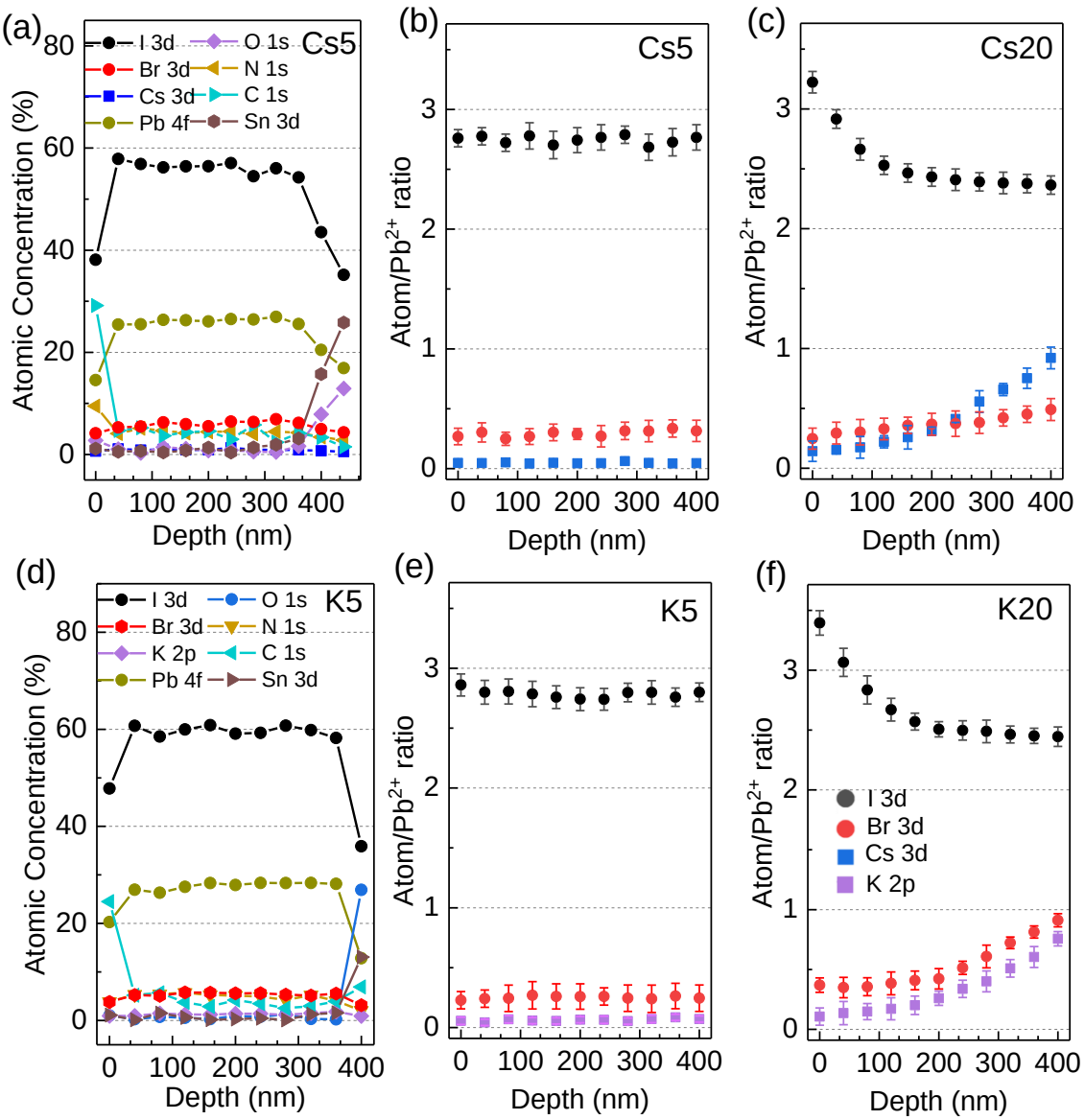

Figure 3. Representative XPS depth profile of Cs^{+}- and K^{+}-incorporated mixed-cation perovskite films, Cs5 (a) and K5 (d). The atomic ratios of the of halides and metal cations relative to lead Pb^{2+} in Cs5 (b), Cs20 (c), K5 (e), and K20 (f). Error bars indicate the standard deviation from averaging the results obtained with different spots.

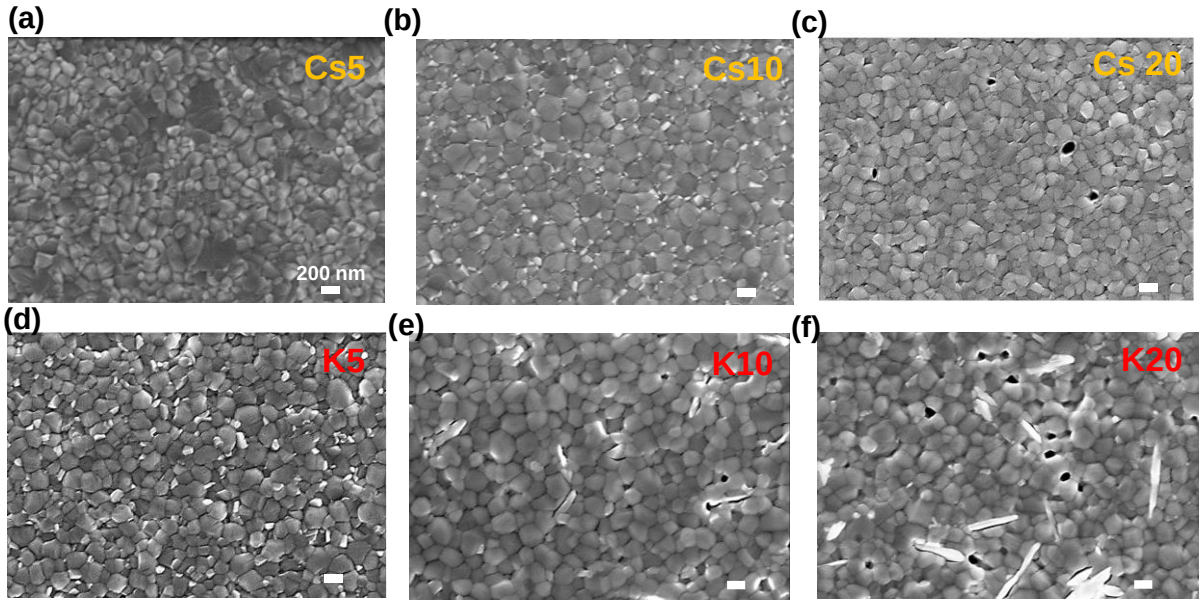

Figure 4. Top-view SEM images of Cs^+- and K^+-containing perovskite solid-state thin films, (a) Cs5, (b) Cs10, (c) Cs20, (d) K5, (e) K10, (f) K20. The horizontal scale bar is 200 nm.

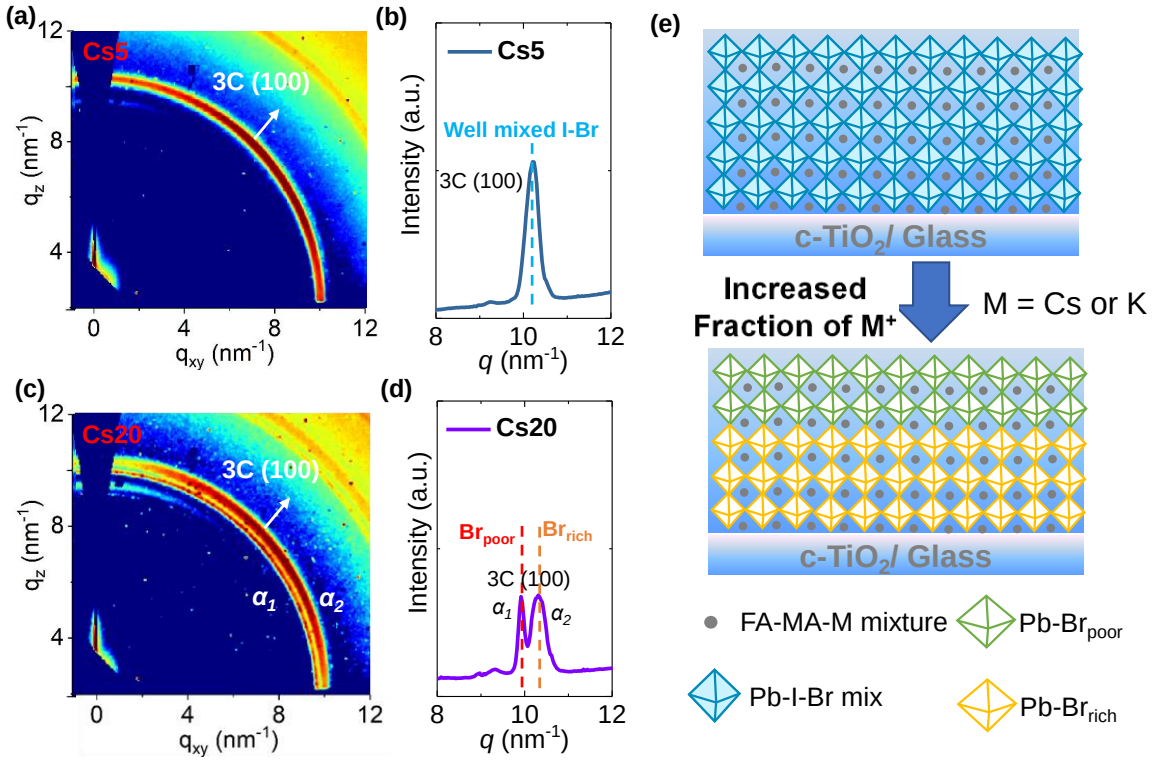

Figure 5. 2D GIWAXS snapshots taken at the final stage of the solution process after thermal annealing together with scattering vector *q* versus intensity distribution of these perovskite films for (a, b) Cs5 and (c, d) Cs20. Scattering features associated with the Br-poor (q = 9.92 nm^{-1}) and Br-rich (q = 10.28 nm^{-1}) perovskite phases are identified along with the welled halide mixture 3C perovskite phase (100) diffraction (q = 10.21 nm^{-1}). (e) Schematic illustration of the observed phase segregation as the alkali metal cation concentration increases.

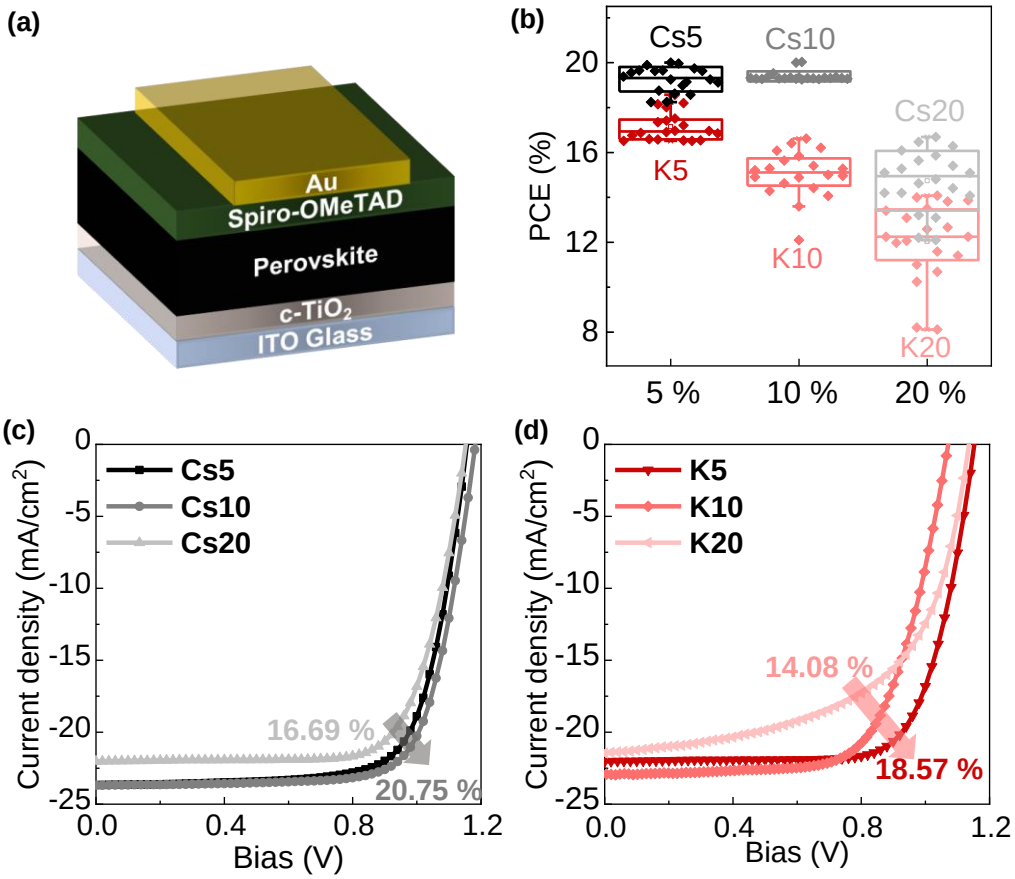

Figure 6. (a) Schematic diagram of the solar cell used in this work. (b) PCEs statistics of 20-25 devices for mixed-cation mixed-halide perovskite solar cells. (c) *J–V* curve for the peak efficiency for Cs5, Cs10, and Cs20 solar cells under AM1.5G illumination. (d) *J–V* curve for the peak efficiency for K5, K10, and K20 solar cells under AM1.5G illumination.

Table 1. Summary of the device parameters of M0, Cs5, Cs10, Cs20 and K5, K10, K20 alkali cations doped mixed-cation mixed-halide perovskite photovoltaics. The results are collected based on the average of 20–30 devices for each condition.[a]

Perovskites		V_{OC} (V)	J_{SC} (mA/cm^2)	*FF* (%)	PCE (%)
M0	Best	1.14	23.01	69.12	18.13
	Average	(1.11 ± 0.04)	(22.72 ± 0.70)	(67.22 ± 3.01)	(16.88 ± 0.84)
Cs5	Best	1.16	23.02	75.15	20.05
	Average	(1.12 ± 0.01)	(22.77 ± 0.27)	(75.50 ± 1.92)	(19.24 ± 0.53)
Cs10	Best	1.18	23.68	74.26	20.75
	Average	(1.14 ± 0.03)	(22.80 ± 0.58)	(75.08 ± 0.89)	(19.45 ± 0.40)
Cs20	Best	1.11	22.09	68.07	16.69
	Average	(1.11 ± 0.01)	(21.94 ± 0.50)	(60.65 ± 5.34)	(14.63 ± 1.30)
K5	Best	1.11	22.72	71.18	18.57
	Average	(1.06 ± 0.05)	(22.95 ± 0.96)	(70.45 ± 0.92)	(17.15 ± 0.62)
K10	Best	1.07	22.93	67.67	16.62
	Average	(0.98 ± 0.05)	(22.45 ± 1.34)	(68.74 ± 1.11)	(15.04 ± 1.02)
K20	Best	1.13	21.42	57.90	14.08
	Average	(0.95 ± 0.11)	(22.13 ± 1.9)	(57.27 ± 2.54)	(12.04 ± 1.69)

[a]Top value represents optimal device and bottom value represents average with standard deviation.

ASSOCIATED CONTENT

Supporting Information.

The Supporting Information is available free of charge on the ACS Publications website.

AUTHOR INFORMATION

Corresponding Author

*E-mail: siyuan.zhang@nist.gov (S.Z.).

*E-mail: thomas.anthopoulos@kaust.edu.sa (T.D.A.).

*E-mail: christina.hacker@nist.gov (C.A.H.).

Author Contributions

S. Zhang and M.-C. Tang contributed equally to this work. S. Zhang, M.-C. Tang, T. D. Anthopoulos, and C. A. Hacker conceived and planned the experiments. S. Zhang performed the UPS and XPS measurements. M.-C. Tang prepared the samples and performed the UV-vis and SEM measurements. M.-C. Tang, Y. Fan and K. Zhao performed solar cell fabrication and characterization. R. Li performed the GIWAXS and analyzed the data. N. V. Nguyen measured and simulated the ellipsometry spectra. All authors provided critical feedback and helped shape the research, analysis, and manuscript.

Funding Sources

This work was supported by the National Institute of Standards and Technology (NIST) Financial Assistance Award with Federal Award ID 70NANB16H228, King Abdullah University of Science and Technology (KAUST), and National Natural Science Foundation of China (61974085). Dr. Tang acknowledges support under the Cooperative Research Agreement between the University of Maryland and the National Institute of Standards and Technology Physical Measurement Laboratory, Award 70NANB14H209, through the University of Maryland.

REFERENCES

1. Lee, S.; Tang, M.-C.; Munir, R.; Barrit, D.; Kim, Y.-J.; Kang, R.; Yun, J.-M.; Smilgies, D.-M.; Amassian, A.; Kim, D.-Y., In situ study of the film formation mechanism of organic–inorganic hybrid perovskite solar cells: controlling the solvate phase using an additive system. *J Mater Chem A* **2020**.
2. Lin, Q.; Armin, A.; Nagiri, R. C. R.; Burn, P. L.; Meredith, P., Electro-optics of perovskite solar cells. *Nat. Photon.* **2015,** *9* (2), 106-112.
3. Miyata, A.; Mitioglu, A.; Plochocka, P.; Portugall, O.; Wang, J. T.-W.; Stranks, S. D.; Snaith, H. J.; Nicholas, R. J., Direct measurement of the exciton binding energy and effective masses for charge carriers in organic-inorganic tri-halide perovskites. *Nat. Phys.* **2015,** *11* (7), 582-587.
4. Tang, M.-C.; Fan, Y.; Barrit, D.; Li, R.; Dang, H. X.; Zhang, S.; Magnanelli, T.; Nguyen, N. V.; Heilweil, E. J.; Hacker, C. A.; Smilgies, D.-M.; Zhao, K.; Amassian, A.;

Anthopoulos, T. D., Efficient Hybrid Mixed Ion Perovskite Photovoltaics: In Situ Diagnostics of the Roles of Cesium and Potassium Alkali Cation Addition. *Sol. RRL. n/a* (n/a).
5. Hao, F.; Stoumpos, C. C.; Chang, R. P.; Kanatzidis, M. G., Anomalous band gap behavior in mixed Sn and Pb perovskites enables broadening of absorption spectrum in solar cells. *J. Am. Chem. Soc.* **2014,** *136* (22), 8094-9.
6. Liu, T. H.; Chen, K.; Hu, Q.; Zhu, R.; Gong, Q. H., Inverted Perovskite Solar Cells: Progresses and Perspectives. *Adv Energy Mater* **2016,** *6* (17), 1600457.
7. Gonzalez-Pedro, V.; Juarez-Perez, E. J.; Arsyad, W. S.; Barea, E. M.; Fabregat-Santiago, F.; Mora-Sero, I.; Bisquert, J., General working principles of CH3NH3PbX3 perovskite solar cells. *Nano Lett.* **2014,** *14* (2), 888-93.
8. Baikie, T.; Fang, Y. N.; Kadro, J. M.; Schreyer, M.; Wei, F. X.; Mhaisalkar, S. G.; Graetzel, M.; White, T. J., Synthesis and crystal chemistry of the hybrid perovskite (CH3NH3) PbI3 for solid-state sensitised solar cell applications. *J Mater Chem A* **2013,** *1* (18), 5628-5641.
9. Zhong, Y.; Munir, R.; Li, J.; Tang, M.-C.; Niazi, M. R.; Smilgies, D.-M.; Zhao, K.; Amassian, A., Blade-Coated Hybrid Perovskite Solar Cells with Efficiency > 17%: An In Situ Investigation. *ACS Energy Lett.* **2018,** *3* (5), 1078-1085.
10. Laboratory, N. R. E. Best Research-Cell Efficiencies Chart. https://www.nrel.gov/pv/assets/pdfs/best-research-cell-efficiencies-190416.pdf (accessed 2019 December).
11. Eperon, G. E.; Stranks, S. D.; Menelaou, C.; Johnston, M. B.; Herz, L. M.; Snaith, H. J., Formamidinium lead trihalide: a broadly tunable perovskite for efficient planar heterojunction solar cells. *Energy Environ. Sci.* **2014,** *7* (3), 982-988.
12. Bush, K. A.; Frohna, K.; Prasanna, R.; Beal, R. E.; Leijtens, T.; Swifter, S. A.; McGehee, M. D., Compositional engineering for efficient wide band gap perovskites with improved stability to photoinduced phase segregation. *ACS Energy Lett.* **2018,** *3* (2), 428-435.
13. Jeon, N. J.; Noh, J. H.; Yang, W. S.; Kim, Y. C.; Ryu, S.; Seo, J.; Seok, S. I., Compositional engineering of perovskite materials for high-performance solar cells. *Nature* **2015,** *517* (7535), 476.
14. Bi, D.; Tress, W.; Dar, M. I.; Gao, P.; Luo, J.; Renevier, C.; Schenk, K.; Abate, A.; Giordano, F.; Baena, J.-P. C., Efficient luminescent solar cells based on tailored mixed-cation perovskites. *Sci. Adv.* **2016,** *2* (1), e1501170.
15. Saliba, M.; Matsui, T.; Seo, J.-Y.; Domanski, K.; Correa-Baena, J.-P.; Nazeeruddin, M. K.; Zakeeruddin, S. M.; Tress, W.; Abate, A.; Hagfeldt, A., Cesium-containing triple cation perovskite solar cells: improved stability, reproducibility and high efficiency. *Energy Environ. Sci.* **2016,** *9* (6), 1989-1997.
16. Wang, K.; Tang, M. C.; Dang, H. X.; Munir, R.; Barrit, D.; De Bastiani, M.; Aydin, E.; Smilgies, D. M.; De Wolf, S.; Amassian, A., Kinetic Stabilization of the Sol-Gel State in Perovskites Enables Facile Processing of High-Efficiency Solar Cells. *Adv. Mater.* **2019,** *31* (32), e1808357.
17. Deepa, M.; Salado, M.; Calio, L.; Kazim, S.; Shivaprasad, S. M.; Ahmad, S., Cesium power: low Cs(+) levels impart stability to perovskite solar cells. *Phys. Chem. Chem. Phys.* **2017,** *19* (5), 4069-4077.
18. Kubicki, D. J.; Prochowicz, D.; Hofstetter, A.; Zakeeruddin, S. M.; Gratzel, M.; Emsley, L., Phase Segregation in Cs-, Rb- and K-Doped Mixed-Cation (MA)x(FA)1-xPbI3 Hybrid Perovskites from Solid-State NMR. *J. Am. Chem. Soc.* **2017,** *139* (40), 14173-14180.

19. Abdi-Jalebi, M.; Andaji-Garmaroudi, Z.; Cacovich, S.; Stavrakas, C.; Philippe, B.; Richter, J. M.; Alsari, M.; Booker, E. P.; Hutter, E. M.; Pearson, A. J.; Lilliu, S.; Savenije, T. J.; Rensmo, H.; Divitini, G.; Ducati, C.; Friend, R. H.; Stranks, S. D., Maximizing and stabilizing luminescence from halide perovskites with potassium passivation. *Nature* **2018,** *555* (7697), 497-501.
20. Son, D. Y.; Kim, S. G.; Seo, J. Y.; Lee, S. H.; Shin, H.; Lee, D.; Park, N. G., Universal Approach toward Hysteresis-Free Perovskite Solar Cell via Defect Engineering. *J. Am. Chem. Soc.* **2018,** *140* (4), 1358-1364.
21. Samu, G. F.; Janaky, C.; Kamat, P. V., A Victim of Halide Ion Segregation. How Light Soaking Affects Solar Cell Performance of Mixed Halide Lead Perovskites. *ACS Energy Lett.* **2017,** *2* (8), 1860-1861.
22. Kubicki, D. J.; Prochowicz, D.; Hofstetter, A.; Zakeeruddin, S. M.; Grätzel, M.; Emsley, L., Phase Segregation in Cs-, Rb- and K-Doped Mixed-Cation (MA)x(FA)1–xPbI3 Hybrid Perovskites from Solid-State NMR. *J. Am. Chem. Soc.* **2017,** *139* (40), 14173-14180.
23. Yoon, S. J.; Kuno, M.; Kamat, P. V., Shift happens. How halide ion defects influence photoinduced segregation in mixed halide perovskites. *ACS Energy Lett.* **2017,** *2* (7), 1507-1514.
24. Barker, A. J.; Sadhanala, A.; Deschler, F.; Gandini, M.; Senanayak, S. P.; Pearce, P. M.; Mosconi, E.; Pearson, A. J.; Wu, Y.; Srimath Kandada, A. R., Defect-assisted photoinduced halide segregation in mixed-halide perovskite thin films. *ACS Energy Lett.* **2017,** *2* (6), 1416-1424.
25. Jiang, Y.; Leyden, M. R.; Qiu, L.; Wang, S.; Ono, L. K.; Wu, Z.; Juarez‐Perez, E. J.; Qi, Y., Combination of Hybrid CVD and Cation Exchange for Upscaling Cs‐Substituted Mixed Cation Perovskite Solar Cells with High Efficiency and Stability. *Adv. Funct. Mater.* **2018,** *28* (1), 1703835.
26. Wang, J.; Qin, M.; Tao, H.; Ke, W.; Chen, Z.; Wan, J.; Qin, P.; Xiong, L.; Lei, H.; Yu, H., Performance enhancement of perovskite solar cells with Mg-doped TiO2 compact film as the hole-blocking layer. *Appl. Phys. Lett.* **2015,** *106* (12), 121104.
27. Tang, Z.; Bessho, T.; Awai, F.; Kinoshita, T.; Maitani, M. M.; Jono, R.; Murakami, T. N.; Wang, H.; Kubo, T.; Uchida, S., Hysteresis-free perovskite solar cells made of potassium-doped organometal halide perovskite. *Sci. Rep.* **2017,** *7* (1), 12183.
28. Xie, H.; Liu, X.; Lyu, L.; Niu, D.; Wang, Q.; Huang, J.; Gao, Y., Effects of precursor ratios and annealing on electronic structure and surface composition of CH3NH3PbI3 perovskite films. *J. Phys. Chem. C* **2015,** *120* (1), 215-220.
29. Liu, L.; McLeod, J. A.; Wang, R.; Shen, P.; Duhm, S., Tracking the formation of methylammonium lead triiodide perovskite. *Appl. Phys. Lett.* **2015,** *107* (6), 061904.
30. Fan, Y.; Qin, H.; Ye, W.; Liu, M.; Huang, F.; Zhong, D., Improving the stability of methylammonium lead iodide perovskite solar cells by cesium doping. *Thin Solid Films* **2018,** *667*, 40-47.
31. Correa-Baena, J.-P.; Luo, Y.; Brenner, T. M.; Snaider, J.; Sun, S.; Li, X.; Jensen, M. A.; Hartono, N. T. P.; Nienhaus, L.; Wieghold, S., Homogenized halides and alkali cation segregation in alloyed organic-inorganic perovskites. *Science* **2019,** *363* (6427), 627-631.
32. Li, Z.; Yang, M.; Park, J.-S.; Wei, S.-H.; Berry, J. J.; Zhu, K., Stabilizing perovskite structures by tuning tolerance factor: formation of formamidinium and cesium lead iodide solid-state alloys. *Chem. Mater.* **2016,** *28* (1), 284-292.
33. Zhang, H.; Fu, X.; Tang, Y.; Wang, H.; Zhang, C.; Yu, W. W.; Wang, X.; Zhang, Y.; Xiao, M., Phase segregation due to ion migration in all-inorganic mixed-halide perovskite nanocrystals. *Nat. Commun.* **2019,** *10* (1), 1088.

34. Slotcavage, D. J.; Karunadasa, H. I.; McGehee, M. D., Light-Induced Phase Segregation in Halide-Perovskite Absorbers. *ACS Energy Lett.* **2016,** *1* (6), 1199-1205.
35. Tang, M. C.; Barrit, D.; Munir, R.; Li, R. P.; Barbe, J. M.; Smilgies, D. M.; Del Gobbo, S.; Anthopoulos, T. D.; Amassian, A., Bismuth-Based Perovskite-Inspired Solar Cells: In Situ Diagnostics Reveal Similarities and Differences in the Film Formation of Bismuth- and Lead-Based Films. *Sol Rrl* **2019,** *3* (7), 1800305.
36. Zhang, Y.; Wang, P.; Tang, M.-C.; Barrit, D.; Ke, W.; Liu, J.; Luo, T.; Liu, Y.; Niu, T.; Smilgies, D.-M.; Yang, Z.; Liu, Z.; Jin, S.; Kanatzidis, M. G.; Amassian, A.; Liu, S. F.; Zhao, K., Dynamical Transformation of Two-Dimensional Perovskites with Alternating Cations in the Interlayer Space for High-Performance Photovoltaics. *J. Am. Chem. Soc.* **2019,** *141* (6), 2684-2694.
37. Barrit, D.; Cheng, P.; Tang, M.-C.; Wang, K.; Dang, H.; Smilgies, D.-M.; Liu, S. F.; Anthopoulos, T. D.; Zhao, K.; Amassian, A., Impact of the Solvation State of Lead Iodide on Its Two-Step Conversion to MAPbI3: An In Situ Investigation. *Adv. Funct. Mater.* **2019,** *0* (0), 1807544.
38. Niu, T.; Lu, J.; Tang, M.-C.; Barrit, D.; Smilgies, D.-M.; Yang, Z.; Li, J.; Fan, Y.; Luo, T.; McCulloch, I.; Amassian, A.; Liu, S.; Zhao, K., High performance ambient-air-stable FAPbI3 perovskite solar cells with molecule-passivated Ruddlesden–Popper/3D heterostructured film. *Energy Environ. Sci.* **2018,** *11* (12), 3358-3366.
39. Tang, M.-C.; Fan, Y.; Barrit, D.; Chang, X.; Dang, H. X.; Li, R.; Wang, K.; Smilgies, D.-M.; Liu, S.; De Wolf, S.; Anthopoulos, T. D.; Zhao, K.; Amassian, A., Ambient blade coating of mixed cation, mixed halide perovskites without dripping: in situ investigation and highly efficient solar cells. *J Mater Chem A* **2020,** *8* (3), 1095-1104.
40. Fan, Y.; Fang, J.; Chang, X.; Tang, M.-C.; Barrit, D.; Xu, Z.; Jiang, Z.; Wen, J.; Zhao, H.; Niu, T.; Smilgies, D.-M.; Jin, S.; Liu, Z.; Li, E. Q.; Amassian, A.; Liu, S.; Zhao, K., Scalable Ambient Fabrication of High-Performance CsPbI2Br Solar Cells. *Joule* **2019,** *3* (10), 2485-2502.
41. Niu, T.; Lu, J.; Jia, X.; Xu, Z.; Tang, M.-C.; Barrit, D.; Yuan, N.; Ding, J.; Zhang, X.; Fan, Y.; Luo, T.; Zhang, Y.; Smilgies, D.-M.; Liu, Z.; Amassian, A.; Jin, S.; Zhao, K.; Liu, S., Interfacial Engineering at the 2D/3D Heterojunction for High-Performance Perovskite Solar Cells. *Nano Lett.* **2019,** *19* (10), 7181-7190.
42. Perez, L. A.; Chou, K. W.; Love, J. A.; van der Poll, T. S.; Smilgies, D. M.; Nguyen, T. Q.; Kramer, E. J.; Amassian, A.; Bazan, G. C., Solvent additive effects on small molecule crystallization in bulk heterojunction solar cells probed during spin casting. *Adv. Mater.* **2013,** *25* (44), 6380-4.
43. Zhong, Y.; Munir, R.; Balawi, A. H.; Sheikh, A. D.; Yu, L.; Tang, M.-C.; Hu, H.; Laquai, F.; Amassian, A., Mesostructured Fullerene Electrodes for Highly Efficient n–i–p Perovskite Solar Cells. *ACS Energy Lett.* **2016,** *1* (5), 1049-1056.
44. Barrit, D.; Cheng, P.; Darabi, K.; Tang, M.-C.; Smilgies, D.-M.; Liu, S.; Anthopoulos, T. D.; Zhao, K.; Amassian, A., Room-Temperature Partial Conversion of α-FAPbI3 Perovskite Phase via PbI2 Solvation Enables High-Performance Solar Cells. *Adv. Funct. Mater.* **2020,** *30* (11), 1907442.
45. Schlipf, J.; Müller-Buschbaum, P., Structure of Organometal Halide Perovskite Films as Determined with Grazing-Incidence X-Ray Scattering Methods. *Adv Energy Mater* **2017,** *7* (16), 1700131.

46. Gratia, P.; Zimmermann, I.; Schouwink, P.; Yum, J.-H.; Audinot, J.-N.; Sivula, K.; Wirtz, T.; Nazeeruddin, M. K., The Many Faces of Mixed Ion Perovskites: Unraveling and Understanding the Crystallization Process. *ACS Energy Lett.* **2017,** *2* (12), 2686-2693.
47. Dang, H. X.; Wang, K.; Ghasemi, M.; Tang, M. C.; De Bastiani, M.; Aydin, E.; Dauzon, E.; Barrit, D.; Peng, J.; Smilgies, D. M.; De Wolf, S.; Amassian, A., Multi-cation Synergy Suppresses Phase Segregation in Mixed-Halide Perovskites. *Joule* **2019,** *3* (7), 1746-1764.
48. Ramsdell, L. S., Studies on Silicon Carbide. *Am Mineral* **1947,** *32* (1-2), 64-82.
49. *All the commercial instruments and materials mentioned here are identified to foster understanding. Such identification does not imply recommendation or endorsement by the National Institute of Standards and Technology, nor does it imply that the materials or equipment identified are necessarily the best available for the purpose.*
50. Speros, J. C.; Martinez, H.; Paulsen, B. D.; White, S. P.; Bonifas, A. D.; Goff, P. C.; Frisbie, C. D.; Hillmyer, M. A., Effects of Olefin Content and Alkyl Chain Placement on Optoelectronic and Morphological Properties in Poly(thienylene vinylenes). *Macromolecules* **2013,** *46* (13), 5184-5194.

ToC figure

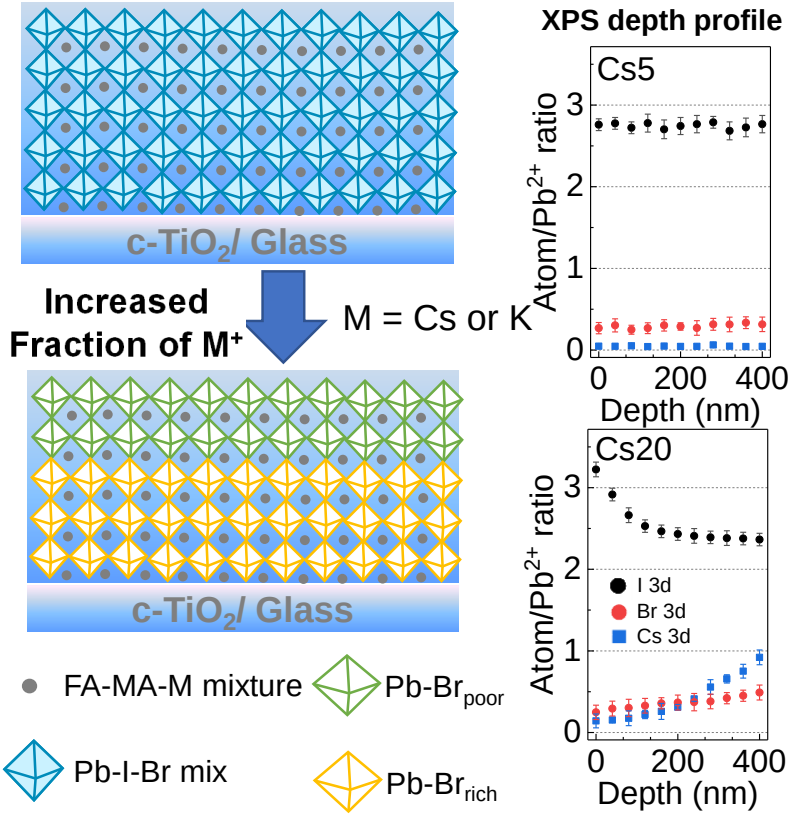
c-TiO2/ Glass
Increased
Fraction of M+
M = Cs or K
c-TiO2/ Glass
FA-MA-M mixture
Pb-Br poor
Pb-I-Br mix
Pb-Br rich
XPS depth profile
Cs5
Atom/Pb2+ ratio
Depth (nm)
Cs20
I 3d
Br 3d
Cs 3d